Zn-doped Fe_2TiO_5 Pseudobrookite-based Photoanodes Grown by Aerosol-Assisted Chemical Vapor Deposition

Miriam Regue,[†,‡,#] Ibbi Y. Ahmet,[§] Prince Saurabh Bassi,[§*] Andrew L. Johnson,[‖] Sebastian Fiechter,[§] Roel van de Krol,[§] Fatwa F. Abdi,[§] and Salvador Eslava[#*]

[†]Centre for Sustainable Chemical Technologies. University of Bath, Claverton Down, Bath, BA2 7AY, United Kingdom.

[‡]Department of Chemical Engineering, University of Bath, Claverton Down, Bath, BA2 7AY, United Kingdom.

[§]Helmholtz-Zentrum Berlin für Materialien und Energie GmbH, Institute for Solar Fuels, Hahn-Meitner-Platz 1, Berlin 14109, Germany.

[‖]Department of Chemistry, University of Bath, Claverton Down, Bath, BA2 7AY, United Kingdom

[#]Department of Chemical Engineering, Imperial College London, London, SW7 2AZ, United Kingdom.

KEYWORDS photoanode, Fe_2TiO_5, Zn-doping, aerosol-assisted chemical vapor deposition, photoelectrochemical.

ABSTRACT: Water splitting in photoelectrochemical cells is a promising technology to produce solar hydrogen. Fe_2TiO_5 pseudobrookite with a bandgap of around 2 eV absorbs the predominant visible range of the solar spectrum and is emerging as a promising photoanode for such cells. Herein, we present Fe_2TiO_5 pseudobrookite-based films prepared by aerosol-assisted chemical vapor deposition and the positive impact of Zn^{2+} doping in their formation and performance. Undoped and Zn^{2+}-doped Fe_2TiO_5 pseudobrookite-based photoanodes were characterized by techniques such as XRD, XPS, UPS and Mott-Schottky analysis. We find that the Zn^{2+} ions are preferentially incorporated in the pseudobrookite phase over a present secondary hematite (α-Fe_2O_3) phase. The Zn^{2+} doping modifies the electronic properties of the films, increases their charge carrier concentration and upshifts their Fermi level, significantly improving their anodic photocurrent response by a factor of three. In addition, charge transfer efficiency calculations reveal that Zn^{2+} doping improves both charge separation and injection efficiencies, overall demonstrating a promising approach for the design of enhanced pseudobrookite-based photoanodes.

INTRODUCTION

A recent report by the Intergovernmental Panel on Climate Change (IPCC) highlighted the urgent need for changing our current energy portfolio, which is highly based on fossil fuels, to a more sustainable one where solar energy plays a key role.[1] Solar energy is abundant, reaching the Earth's surface at approximately 3.4 x 10^{24} J per year, but there is still a need to develop technologies such as photoelectrochemical (PEC) water splitting to store this intermittent energy in the form of chemical bonds, known as solar fuels.[2] Since its first discovery in 1972 by Fujishima and Honda on TiO_2 photoanodes[3] other types of materials such as Fe_2O_3, WO_3, $BiVO_4$, TaON, GaP and Ta_3N_5 have been investigated.[4,5] Metal oxides are the most promising type of materials owing to its semiconductor nature and good chemical stability in aqueous solutions. However, their reported efficiencies are still low and far from commercialization. The lack of existing materials able to meet the requirements for PEC applications is triggering the research community to look for unique material combinations and architectures that would satisfy the challenging requirements of PEC. Nanostructuring, doping, electrocatalyst loading, building heterostructures or combining molecular catalysts with semiconductors are among the most innovative approaches to improve PEC performances.[6–8]

Among the various light-harvesting materials used in PEC devices, iron titanate pseudobrookite (Fe_2TiO_5), a hybrid of Fe_2O_3 and TiO_2 with Fe-O-Ti bonds, is a promising *n-type* semiconductor with a bandgap of 1.9-2.1 eV and abundant metal sources.[9,10] Although a promising material at a glance, its development has been hindered by its difficulty to synthesize and the lack of knowledge of its properties.

In 2014, Courtin *et al.* developed a sol-gel synthesis and a dip coating process, reporting for the first time the Fe_2TiO_5 phase in thin films.[11] Up to three different phases were identified in the final films — anatase (TiO_2), hematite (α-Fe_2O_3) and Fe_2TiO_5 pseudobrookite— and their relative amounts depended on the ratio of Fe:Ti used in the precursors. Alternatively, Bassi *et al.* synthesized a pure phase of Fe_2TiO_5 using a solvothermal method and demonstrated its conduction and valence band edge positions were suitable for water splitting applications.[10] Very recently, Bassi *et al.* also reported for the first time Fe_2TiO_5 photoanodes grown by pulsed laser deposition.[12] Lee *et al.* reported a novel electrochemical method based on the use of metal-catechol complexes for the fabrication of pure Fe_2TiO_5 photoanodes.[13] Kuang *et al.* reported an electrospray technique for the preparation of Fe_2TiO_5 photoanodes and posteriorly modified them by surface state passivation with Al^{3+} and by FeOOH decoration, showing both approaches were effective in increasing the resulting photocurrent density values to 0.52 mA cm^{-2} at +1.23 V_{RHE}.[14] Similarly, Wang *et al.* carried out a F-surface treatment of Fe_2TiO_5 and increased photocurrent density values due to formation of Ti-F facilitating hole transfer to the electrolyte.[15]

The multi-step deposition of thin layers of Fe_2TiO_5 on top of TiO_2 or α-Fe_2O_3 has also been researched. In 2014 Liu *et al.* reported the synthesis of Fe_2TiO_5 and a CoO_x catalyst on top of aligned TiO_2 nanotubes grown by electrochemical deposition.[16] This increased the incident-photon-to-current efficiency at 400 nm and +1.23 V_{RHE} from 5 to 40 %, showing this staggered structure can result in anisotropic charge carrier transport and reduced charge carrier transfer resistance.[16] Similarly, a second deposition of a thin layer of Fe_2TiO_5 on α-Fe_2O_3 photoanodes also successfully enhanced

the IPCE of pristine α-Fe_2O_3 photoanodes due to improved charge transfer.[17–19]

Aerosol-assisted chemical vapor deposition (AACVD) is a deposition technique that has gained great interest in the fabrication of thin films for PEC applications mainly because it can produce large-area robust films with good reproducibility and relatively low processing cost, which would help in the fabrication of a large-scale PEC device.[20–22]

In this publication, we report the AACVD of Fe_2TiO_5 pseudobrookite-based films and the impact of Zn doping. We have designed a stable precursor solution enabling the composition of titanium (IV) isopropoxide, iron (III) acetylacetonate and zinc acetate dihydrate in a single solution mixture with ethyl acetate and methanol as solvents. From this precursor solution, we demonstrate the deposition of a homogeneous coating on a large substrate area (length of 20 cm) from a single aerosol outlet. X-ray diffraction of the deposited films reveals that Zn^{2+} doping boosts the formation of the Fe_2TiO_5 pseudobrookite phase. Moreover, Zn^{2+} ions preferentially occupy the Fe_2TiO_5 pseudobrookite phase over an existing α-Fe_2O_3 secondary phase. Characterization techniques such as X-ray photoelectron spectroscopy, electrochemical impedance spectroscopy and ultraviolet photoelectron spectroscopy reveal that the addition of Zn^{2+} significantly modifies the electronic properties of the films, by upshifting the Fermi level (E_F) and enhancing the electron carrier density (N_d). When these films are studied as photoanodes in PEC cells, the Zn^{2+} doping contributes to an overall enhancement of both the charge separation and injection efficiencies, which triples their photocurrent density response under simulated sunlight. These results emphasize the importance of tuning the electronic properties of Fe_2TiO_5 pseudobrookite with dopants to realize its potential.

EXPERIMENTAL

Materials

Titanium (IV) isopropoxide, iron (III) acetylacetonate, zinc acetate dihydrate, ethyl acetate and methanol were used as received from Sigma Aldrich. Fluorine doped tin oxide (FTO) coated glass (TEC 7) was provided by Pilkington and cut in 2.5 cm-wide and 30 cm-long substrates, for their use in the AACVD system. These substrates were cleaned ultrasonically with a soap solution (10 vol% Triton X-100), ethanol and deionized water and finally dried with compressed air.

Preparation of Thin Films

All photoanodes were prepared using AACVD on FTO-coated glass and named after their constituent elements (e.g. Fe-Ti-O-Zn and Fe-Ti-O). The aerosol droplets were generated using a TSI Model 3076 Constant Output atomizer using argon as a carrier gas (Figure 1) with the following precursor solutions.[23,24] For Fe-Ti-O films, titanium (IV) isopropoxide (1.478 mL, 5.0 mmol) was dissolved in 10 mL of methanol and mixed together with a solution of iron (III) acetylacetonate (3.531 g, 10 mmol) in 100 mL of ethyl acetate. For Fe-Ti-O-Zn films, zinc acetate dihydrate (0.0549 g, 0.25 mmol) was added to the previous iron and titanium solution, corresponding to a molar percentage of 2.5% compared to Fe. As control experiments, Fe-O and Fe-O-Zn films were also prepared by removing the titanium precursor from the solution but keeping the same stoichiometric and volumetric ratio of precursors and solvents. All samples were deposited for 1 h at 450 °C. The obtained films were annealed in air in two steps: at 500 °C for 12 h and at 650 °C for 2 h. The heating rate was 10 °C min^{-1}. Other Zn concentrations and deposition times were also tried, but either lower performance or phase segregation was obtained; the conditions described here are therefore optimized.

Characterization

X-ray diffraction (XRD) patterns were collected from 10 to 60° (2θ) using a Bruker D8 diffractometer with Cu Kα (0.15406 nm) radiation. Measurements were carried out in a grazing incidence geometry (incidence angle = 0.5°). The coherent diffraction domain sizes of Fe_2TiO_5 were calculated using the Scherrer equation at the 020 and 110 peaks, respectively. Raman spectroscopy was performed with a Renishaw inVia system using a 532 nm diode-pumped solid-state laser (DPSS) manufactured by Cobolt™. A 50x long distance objective was used to focus the laser beam onto the sample. UV-Vis absorption measurements were carried out in a Lambda 950 spectrometer (Perkin Elmer) with an integrating sphere (150 mm). Diffuse-reflectance UV-Vis measurements were performed in an Agilent Cary 100 spectrophotometer. Field-emission scanning electron microscopy micrographs (FE-SEM) were acquired using a LEO/Zeiss Gemini Sigma300 instrument with a Thermo Fisher energy dispersive X-ray (EDX) detector. EDX was performed with an acceleration voltage of 15 kV. X-ray photoelectron spectroscopy (XPS) was performed with a monochromatic Al Kα X-ray source (1486.74 eV, Specs Focus 500 monochromator). Adventitious C 1s was used for internal charge correction. Ultraviolet photoelectron spectroscopy (UPS) was carried out with an He

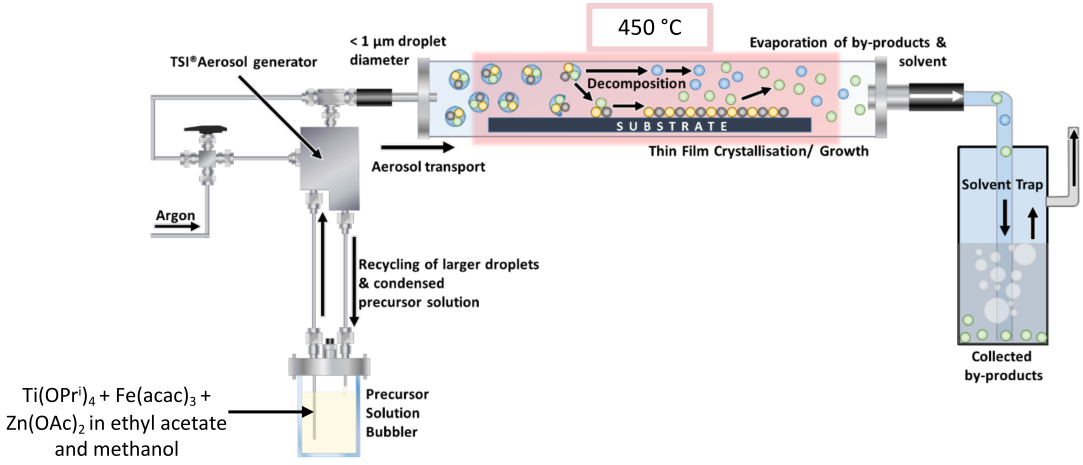

Figure 1. Schematic AA-CVD set-up used in the preparation of all photoanodes.

I source (E = 21.218 eV) in the same system. A hemispherical analyzer (Specs Phoibos 100) was used for both XPS and UPS measurements. The base pressure of the system was ~10^{-9} mbar.

PEC measurements

PEC performance of photoanodes was measured under simulated solar light using a WACOM Super Solar Simulator (Model WXS-505-5H, AM 1.5, Class AAA) and an EG&G Princeton Applied Research Potentiostat/Galvanostat (Model 273A). PEC cells were prepared using a three-electrode configuration with Pt as the counter electrode, a silver chloride reference electrode (Ag/AgCl-reference electrode, saturated KCl, XR300, Radiometer Analytical, $E_{Ag/AgCl}$=0.197 V_{RHE}) and the prepared photoanodes as the working electrode. Illumination was directed from the back of the photoanode via the FTO-coated glass substrate. An aqueous solution of NaOH (1 mol L^{-1}, pH=13.6) was used as the electrolyte. All the measured potentials ($E_{Ag/AgCl}$) were converted to RHE potentials (E_{RHE}) using the Nernst equation. Current-voltage curves for charge injection and charge separation efficiencies were recorded using the above-mentioned configuration, but with the addition of 10% (v/v) of H_2O_2 as a hole scavenger in the aqueous NaOH electrolyte. Charge injection efficiencies were calculated using the following equation:

$$\eta_{inj} = \frac{j_{photo\ (NaOH)}}{j_{photo\ (NaOH+H2O2)}} \quad (1)$$

and charge separation efficiencies were calculated using Equation 2:

$$\eta_{sep} = \frac{j_{photo\ (H2O2+NaOH)}}{j_{abs}} \quad (2)$$

where $j_{photo(NaOH)}$ and $j_{photo(NaOH+H2O2)}$ are the measured photocurrent density values in the aqueous NaOH and NaOH & H_2O_2 electrolytes, respectively. j_{abs} is the theoretical maximum photocurrent density obtained when all the absorbed photons are converted into current density and it is calculated by integrating the absorptance spectra with the standard AM 1.5G spectrum.[19,25]

Incident-photon-to-current efficiency (IPCE) measurements were performed using a Xe lamp (LOT, LSH302), an Acton Research monochromator (Spectra Pro 2155) and an electronic shutter (Uniblitz LS6). The intensity of the monochromatic light arriving at the film under back-side illumination was measured with a calibrated photodiode (PD300R-UV, Ophir) with an FTO-glass substrate placed in front, in the same position of the working electrode, inside the PEC cell with the quartz window and electrolyte removed. The IPCE was calculated using the equation below:

$$IPCE\ (\lambda) = \frac{|j(mA\ cm^{-2})| \times 1239.8\ (V\ nm)}{P_{mono}(mW\ cm^{-2}) \times \lambda\ (nm)} \quad (3)$$

where j is the photocurrent density measured under monochromatic light of wavelength λ and P_{mono} is the incident irradiation power density. Absorbed-photon-to-current efficiency (APCE) was calculated according to:

$$APCE\ (\lambda) = \frac{IPCE(\lambda)}{1-10^{-A(\lambda)}} \quad (4)$$

where $A(\lambda)$ is the absorbance measured at a wavelength λ.

Applied-bias photon-to-current efficiency (ABPCE)] was calculated using Equation 5.[26]

$$ABPCE = j_p \left[\frac{E^{H2O}/_{O2} - E_{app}}{P_{in}}\right] x\ 100 \quad (5)$$

where j_p is the photocurrent density (mA cm^{-2}), $E^{H2O/O2}$ is the standard reversible potential for water oxidation (+1.23 V_{RHE}), E_{app} is the applied potential and P_{in} is the power density of the incident light (mW cm^{-2}).

PEC impedance spectroscopy (PEIS) was carried out under simulated solar light (AM 1.5G, 100 mWcm^{-2}) at +1.23 V_{RHE}, and at a frequency range of 10^5-0.1 Hz with an amplitude of 10 mV.

Electrochemical impedance spectroscopy (EIS) measurements in the dark were also measured to obtain Mott-Schottky plots. These measurements were performed at a fixed frequency (100 Hz). The following equation was used:

$$\frac{1}{C^2} = \frac{2}{N_d e \varepsilon_0 \varepsilon}\left[(E_s - E_{Fb}) - \frac{K_B T}{e}\right] \quad (6)$$

where C is the semiconductor depletion layer capacitance, N_d the electron carrier density, e the elementary charge value, ε_0 the permittivity of the vacuum, ε the relative permittivity of the semiconductor, E_s the applied potential, E_{Fb} the flat band potential, and $[K_BT/e]$ a temperature-dependent correction term. N_D was obtained from the slope of the Mott-Schottky plots, where ε is 100 for Fe_2TiO_5,[10] and $[d(1/C^2)/d(Es)]^{-1}$ is the inverse of the slope obtained from the Mott-Schottky plot.

RESULTS AND DISCUSSION

Fe-Ti-O and Fe-Ti-O-Zn films were grown using AACVD and a homogenous film coverage was obtained across *ca.* 20 cm-long pieces of the FTO-coated glass substrates (Figure S1†). As-deposited films are black in color due to carbon residues coming from the solvent and chemical precursors used (Figure S1†) and they are also amorphous (see for example Fe-Ti-O films in Figure S2†). After annealing them in air at 500 °C and subsequently at 650 °C crystalline films are obtained. Figure 2a shows their XRD patterns. Fe-Ti-O shows the characteristic diffraction peaks of Fe_2TiO_5 pseudobrookite (JCPDS 009-0182) along with some diffraction peaks of α-Fe_2O_3 (JCPDS 006-0502) and TiO_2 rutile (diffraction peak at 27.6°, JCPDS 88-1173). A broad peak at 2 θ ≈ 56° corresponding to $Fe_{1.7}Ti_{0.23}O_3$ is also present.[27] The main diffraction peaks at 2 θ ≈ 18, 25.5, 32.7 and 41.1° correspond to the 020, 110, 023 and 042 XRD peak positions of Fe_2TiO_5 pseudobrookite, respectively. Incorporation of Zn^{2+} for Fe-Ti-O-Zn samples leads to more intense pseudobrookite phase peaks, narrower α-Fe_2O_3 diffraction peaks, and the disappearance of the TiO_2 rutile and $Fe_{1.7}Ti_{0.23}O_3$ diffraction peaks. No diffraction peaks corresponding to ZnO or $ZnFe_2O_4$ are observed for Fe-Ti-O-Zn films, suggesting that Zn^{2+} is either homogeneously dissolved in the solid, accumulated in amorphous regions, or the amount is too small to be detected by XRD. Figure 2b shows the close-up of the 110 diffraction peaks for Fe_2TiO_5 and Figure 2c the 104 and 110 diffraction peaks for α-Fe_2O_3, obtained from the Fe-Ti-O and Fe-Ti-O-Zn films. Interestingly, the addition of Zn^{2+} shifted the 110 Fe_2TiO_5 diffraction peak from 25.54 to 25.31°, but did not shift the 104 nor the 110 diffraction peak of α-Fe_2O_3, revealing the incorporation of Zn^{2+} in the crystal lattice happens mainly in the pseudobrookite phase. The 110 pseudobrookite peak (Figure 2b) can be deconvoluted in two peaks at 25.4 and 25.6° belonging to two pseudobrookite phases of slightly different compositions ($Fe_{1+x}Ti_{2-x}O_5$ ($0 \le x \le 1$)). With the Zn^{2+} incorporation, the intensity of the lower-incidence-angle peaks are enhanced whilst the larger-incidence-angle peaks almost vanish.

The lattice parameters calculated from the XRD patterns are shown in Table 1. Lattice parameters varied remarkably. Considering an orthorhombic compound that crystallizes in the space group *Cmcm* as known for pseudobrookite films, the addition of Zn^{2+} leads to an increase of the *a* and *b* lattice parameters but a shrinkage of the *c* axis value. The change of the lattice constants in Fe-Ti-O and Fe-Ti-O-Zn systems can be explained by a higher degree of cation disorder in the pseudobrookite crystal structure after introducing Zn^{2+} cations.[28,29] From a structural point of view,

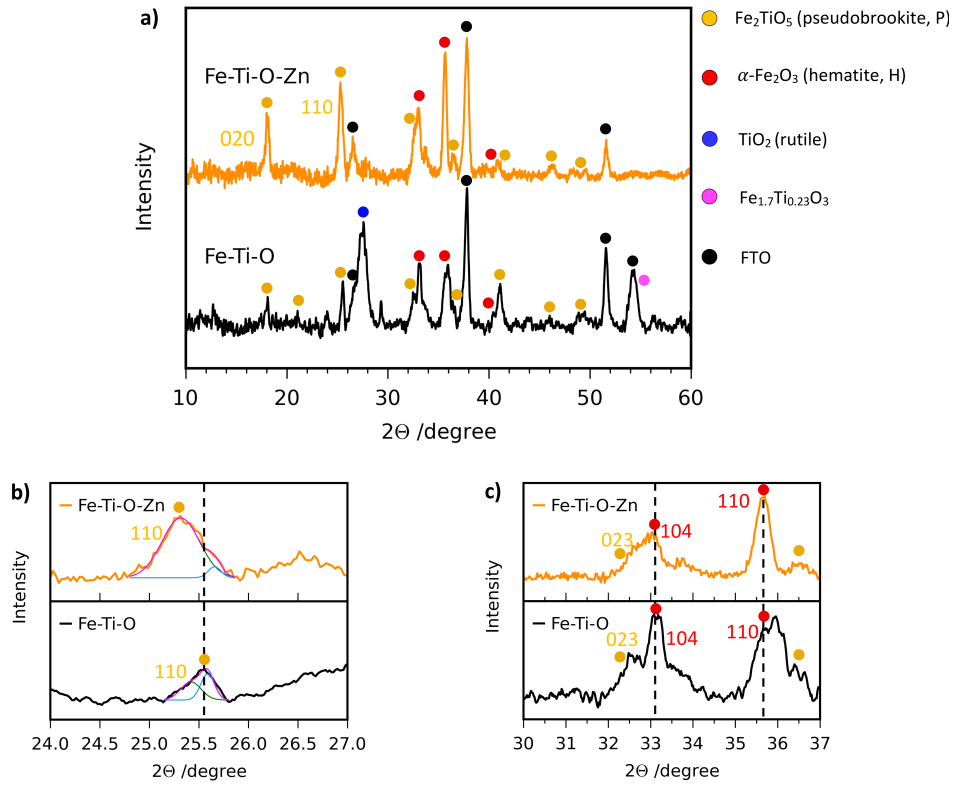

Figure 2. (a) XRD patterns of Fe-Ti-O-Zn and Fe-Ti-O. Yellow dot: Fe_2TiO_5, red dot: α-Fe_2O_3, blue dot: TiO_2 rutile, pink dot: $Fe_{1.7}Ti_{0.23}O_3$ and black dot: FTO. (b) Close-up XRD diffraction profile of the (b) Fe_2TiO_5 pseudobrookite 110 peak and of the (c) α-Fe_2O_3 104 and 110 peaks for Fe-Ti-O samples.

those lattice changes are correlated with variations in the cation (Fe, Ti)-oxygen bond length of corner-sharing coordination octahedra in the pseudobrookite lattice.[30] These distortions are caused by the differences in ionic radii between Zn^{2+} (0.74 Å) and that of Ti^{4+} (0.605 Å) as well as Fe^{3+} (0.79 Å) and also Fe^{2+} (0.92 Å) and Ti^{3+} (0.81 Å) that are evidently existing within these films (see XPS results below).[31,32] In addition, the similarity of our calculated *a* and *b* lattice parameters for the Fe-Ti-O-Zn film with those reported by Müller-Buschbaum for a titanium-rich pseudobrookite (*a=3.756* Å and *b=9.812* Å) suggests a titanium-rich composition (small *x* in $Fe_{1+x}Ti_{2-x}O_5$) in the samples.[33] Conversely, our calculated *a* and *b* values for the Fe-Ti-O sample suggest an iron rich pseudobrookite (*x* approaching 1 in $Fe_{1+x}Ti_{2-x}O_5$).[34] However, compositional gradients in the pseudobrookite parts of the films cannot be excluded. In addition, Fe-Ti-O-Zn exhibits a higher cell volume (365.4 Å^3) when compared with Fe-Ti-O (363.5 Å^3). This indicates that Zn^{2+} ions are most likely occupying interstitial positions in the Fe_2TiO_5 lattice. [35,36]

The coherent crystal domain sizes calculated from the 020 diffraction peak of Fe_2TiO_5 in Fe-Ti-O and Fe-Ti-O-Zn films are *ca.* 21 nm. Interestingly, the incorporation of Zn^{2+} does not significantly influence the crystallite size.

Table 1. Calculated lattice parameters.

Sample	*a* (Å)	b (Å)	*c* (Å)	Volume (Å^3)
[a]Fe-Ti-O	3.729	9.801	9.946	363.5
[a]Fe-Ti-O-Zn	3.763	9.824	9.884	365.4

[a] Lattice parameters calculated considering an orthorhombic

Raman spectra of Fe-Ti-O and Fe-Ti-O-Zn are shown in Figure S3†. Bands at 204, 342, 410, 610, 655 and 800 cm^{-1} correspond to the vibrational modes of Fe_2TiO_5 pseudobrookite in Fe-Ti-O and Fe-Ti-O-Zn samples.[16,37–39] The main difference between these two spectra is a change of the intensities of the vibration modes located at 610 and 655 cm^{-1}. The band at 610 cm^{-1} is of higher intensity in Fe-Ti-O than in Fe-Ti-O-Zn films, whereas the band at 655 cm^{-1} is of lower intensity in Fe-Ti-O and becomes predominant in Fe-Ti-O-Zn. The higher intensity of the 655 cm^{-1} band in Fe-Ti-O-Zn is consistent with an increase of the *b* lattice constant observed in the calculated lattice parameters (Table 1) and further confirms the increase of cation disorder in Fe-Ti-O-Zn films when compared with Fe-Ti-O films. Raman bands ascribed to α-Fe_2O_3 are also observed in Fe-Ti-O and Fe-Ti-O-Zn films: bands at 223.7 and 494.4 cm^{-1} corresponding to A_{1g} vibration modes, bands at 243, 290.8, 408.3 and 607.1 cm^{-1} corresponding to E_g vibration modes,[40,41] and a strong band at 1310 cm^{-1} corresponding to a two-magnon Raman scattering.[40] Therefore, the Raman results confirm the presence of pseudobrookite and α-Fe_2O_3, as observed by XRD, and supports cation-disorder characteristics in Fe-Ti-O-Zn films.

UV-Vis absorptance spectra of photoanodes are shown in Figure 3. Undoped Fe-Ti-O exhibits an absorption edge at ~580 nm, whereas the Fe-Ti-O-Zn sample exhibits a red shift of the absorption edge to ~590 nm. Fe-Ti-O-Zn has higher

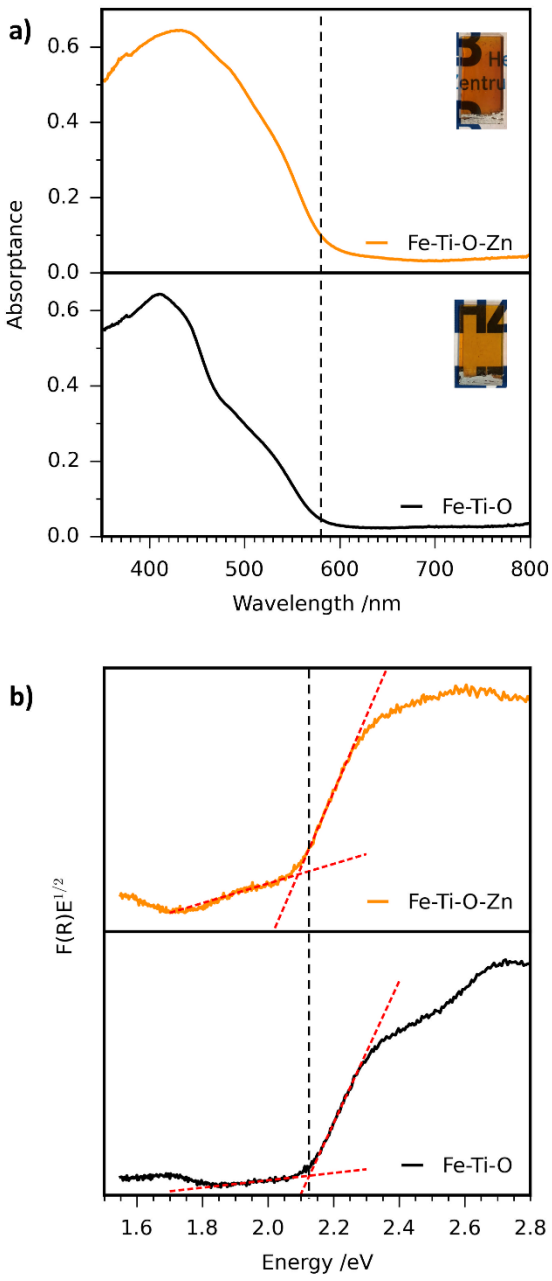

Figure 3. (a) UV-Vis absorptance spectra and (b) Tauc plots measured *via* diffuse reflectance UV-Vis spectroscopy of Fe-Ti-O-Zn and Fe-Ti-O. Insets in (a) show photographs of all photoanodes prepared. Dashed vertical line indicates onsets for Fe-Ti-O. The logo is copyrighted by the Helmholtz-Zentrum Berlin für Materialien und Energie GmbH.

absorption values in agreement with its darker color (see inset of Figure 3a). Accordingly, the Fe-Ti-O-Zn sample possesses a smaller band gap of 2.10 eV, in comparison with 2.13 eV for the undoped Fe-Ti-O sample (Figure 3b). We attribute the slight decrease in the band gap to the formation of a shallow state below the CB with the addition of Zn^{2+}.[32] Band-gap values around 2.1 eV are consistent with previously reported band-gap calculations of Fe_2TiO_5.[10]

Figure 4 shows the FE-SEM micrographs of the top surface of the photoanodes. Fe-Ti-O and Fe-Ti-O-Zn show a

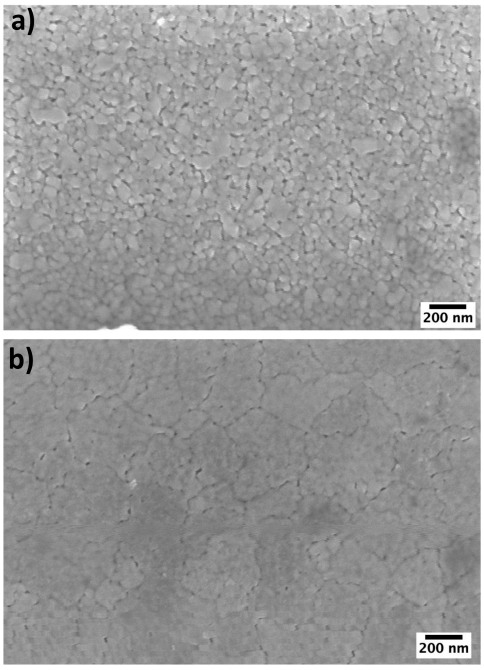

Figure 4. FE-SEM micrographs of (a) Fe-Ti-O and (b) Fe-Ti-O-Zn.

very fine structure consisting of small particles. The addition of Zn^{2+} does not significantly modify the final morphology of the films. Cross-sectional FE-SEM micrographs (Figure S4†) show that the thickness of the films is ~555 and ~400 nm for Fe-Ti-O and Fe-Ti-O-Zn films, respectively. Noticeably, the incorporation of Zn^{2+} results in the formation of more compact films.

The composition and chemical state of the film surfaces were evaluated using XPS analysis. The Zn $2p_{3/2}$ high-resolution XPS spectrum of Fe-Ti-O-Zn is shown in Figure 5a with the main characteristic peak of Zn^{2+} at 1020.3 eV.[42] A binding energy of 1021.0 eV was previously reported for heterostructured Zn 2p in $ZnFeO_4/Fe_2TiO_5/TiO_2$ nanotube arrays, in which $ZnFeO_4$ consists of a spinel structure.[43] These differences in binding energies suggest a different ligand field coordination for Zn^{2+} in the structure. In the case of $ZnFeO_4$, a tetrahedral coordination exists whereas in our Fe-Ti-O-Zn system, an octahedral coordination is expected.[43] XPS survey spectra show that Fe-Ti-O-Zn contain 0.11 at% of Zn^{2+} on the surface (Figure S5†). The presence of Zn^{2+} in Fe-Ti-O-Zn is further confirmed by SEM-EDX (Figure S6†).

Ti 2p high-resolution XPS spectra of Fe-Ti-O and Fe-Ti-O-Zn are shown in Figure 5b and peak positions are listed in Table 2. Fe-Ti-O sample has the two characteristic peaks of Ti^{4+} corresponding to Ti $2p_{1/2}$ and Ti $2p_{3/2}$.[44] Interestingly, Fe-Ti-O-Zn shows a shift of 1.3 eV towards lower binding energies, assigned to a Ti^{3+} oxidation state.[44] This change of oxidation state from Ti^{4+} to Ti^{3+} is usually accompanied by the presence of oxygen vacancies in the film to compensate any charge imbalance introduced into the lattice due to the addition of Zn^{2+}.[35,45,46] This indicates that Zn^{2+} ions are most likely to be occupying Ti^{4+} positions or interstitial sites in the pseudobrookite lattice structure, as also demonstrated

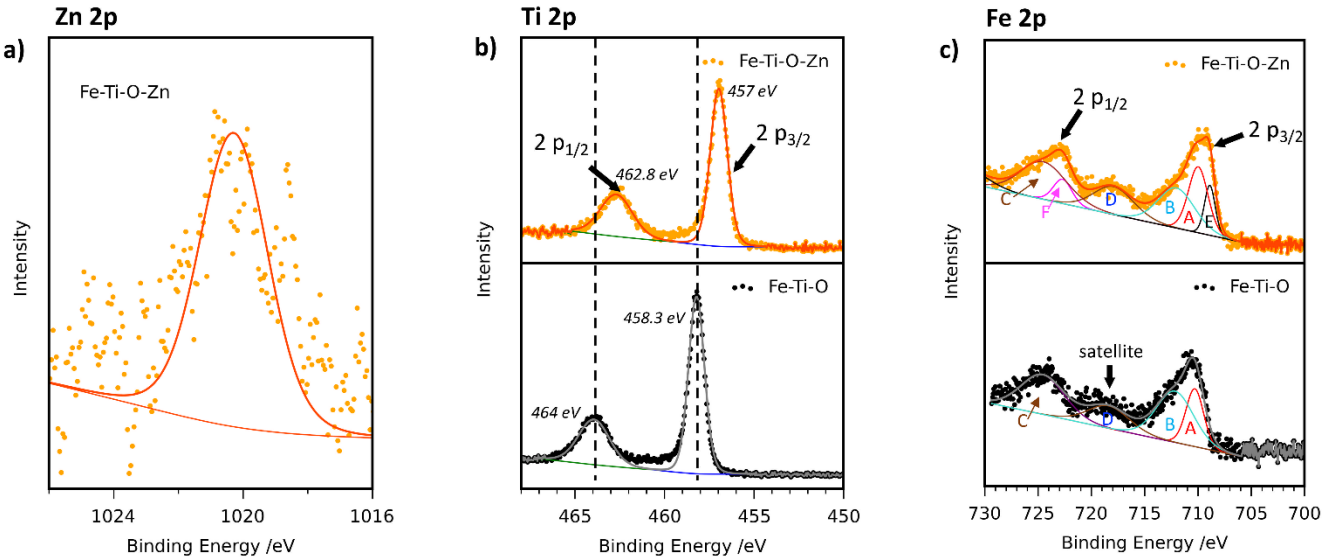

Figure 5. XPS spectra of (a) Zn 2p, (b) Ti 2p and (c) Fe 2p for Fe-Ti-O-Zn and Fe-Ti-O. Scattered points correspond to raw data acquired in the measurements and solid lines to the fitted values.

in the calculated lattice parameters (Table 1) and XRD patterns (Figure 2b,c).[32] Figure 5c shows the Fe 2p high-resolution XPS spectra of Fe-Ti-O and Fe-Ti-O-Zn. Both samples show the characteristic peaks of Fe $2p_{1/2}$ and Fe $2p_{3/2}$ at *ca.* 725 and 710 eV, respectively, along with satellite signals at around 8 eV above the Fe $2p_{3/2}$ (peak D, Figure 5c), corresponding to Fe^{3+}.[47,48] This satellite signal could also correspond to Sn $3p_{3/2}$ core level coming from the FTO in the substrate.[49] Peak fitting analysis of the Fe 2p XPS spectra shows that Fe-O-Ti consists only of Fe^{3+} species (peaks A-C, Figure 5c). However, a substantial contribution of Fe^{2+} appears in the Fe-Ti-O-Zn sample, as demonstrated by the additional peaks required for the fitting (peaks E and F), assigned to Fe^{2+} species.[50] An Fe^{2+}:Fe^{3+} ratio of 0.2:0.8 is estimated from the peak areas of the deconvoluted Fe $2p_{3/2}$ spectra. The presence of Fe^{2+} centers in Fe-Ti-O-Zn suggests that Zn^{2+} might also be occupying octahedrally coordinated sites in the pseudobrookite lattice. A small shift towards lower binding energies is also observed in fitted Fe 2p peaks of Fe-Ti-O-Zn when compared with undoped Fe-Ti-O, as shown in Table 2. However, this shift is significantly smaller in Fe 2p spectra than in Ti 2p spectra. We attribute this to band-bending effects, confirming the formation of a depletion layer after Zn loading.[51–53] The shift observed in the Ti 2p spectrum for Fe-Ti-O-Zn is, therefore, ascribed to a combination of band-bending effects, the presence of Ti^{3+} centers and oxygen vacancies.

Therefore, from XPS along with XRD analysis we suggest that the pseudobrookite phase in Fe-Ti-O-Zn samples can be described as $Fe^{2+}_{0.2}Fe^{3+}_{0.8}(Ti^{3+}_{x}Ti^{4+}_{1-x})_2O_{5-\delta}$ at the surface with Zn^{2+} ions occupying cations (Fe or Ti) sites or octahedrally coordinated interstitial sites of the pseudobrookite phase.

The PEC performance of the photoanodes was evaluated under simulated sunlight for back- and front-side illumination (Figure 6a and Figure S7†, respectively). Back-side illumination measurements show higher PEC performances when compared with front-side illumination measurements, indicating that electron transport is less efficient than hole transport in the films and/or a more effective bias closer to the FTO.[54] Based on this, all further measurements were performed with back-side illumination. The Fe-Ti-O sample shows a photocurrent density value of 0.2 mA cm^{-2} at +1.23 V_{RHE}, but the Fe-Ti-O-Zn sample demonstrates a much higher photocurrent density of 0.6 mA cm^{-2} at +1.23 V_{RHE}, which is an outstanding photocurrent response for an Fe_2TiO_5-based system in which Fe_2TiO_5 is the major phase. We attribute this PEC enhancement to the beneficial effects of Zn doping in the Fe_2TiO_5 pseudobrookite phase. The intimate contact between the major Fe_2TiO_5 phase and the minor α-Fe_2O_3 phase in both Fe-Ti-O and Fe-Ti-O-Zn samples forming a type II- band alignment configuration might also contribute to improve the PEC performance due to charge separation.[11,19] As control experiments, *j-V* curves of films prepared in the absence of Ti were measured and they showed poorer PEC performance (pure hematite Fe-O and Fe-O-Zn films, Figure S8).

Table S1† reports the state of the art of Fe_2TiO_5-based photoanodes. Compared with our Fe-Ti-O-Zn samples,

Table 2. Peak positions used to fit Fe 2p and Ti 2p XPS spectra.

	Ti 2p (eV)		Fe 2p (eV)		
Sample	**$2p_{3/2}$**	**$2p_{1/2}$**	**A**	**B**	**C**
Fe-Ti-O	458.3	464.0	710.3	712.1	724.6
Fe-Ti-O-Zn	457.0	462.8	710.0	712	724.5
ΔE	1.3	1.2	0.3	0.1	0.1

ΔE corresponds to the difference between the undoped sample (Fe-Ti-O) and doped sample (Fe-Ti-O-Zn).

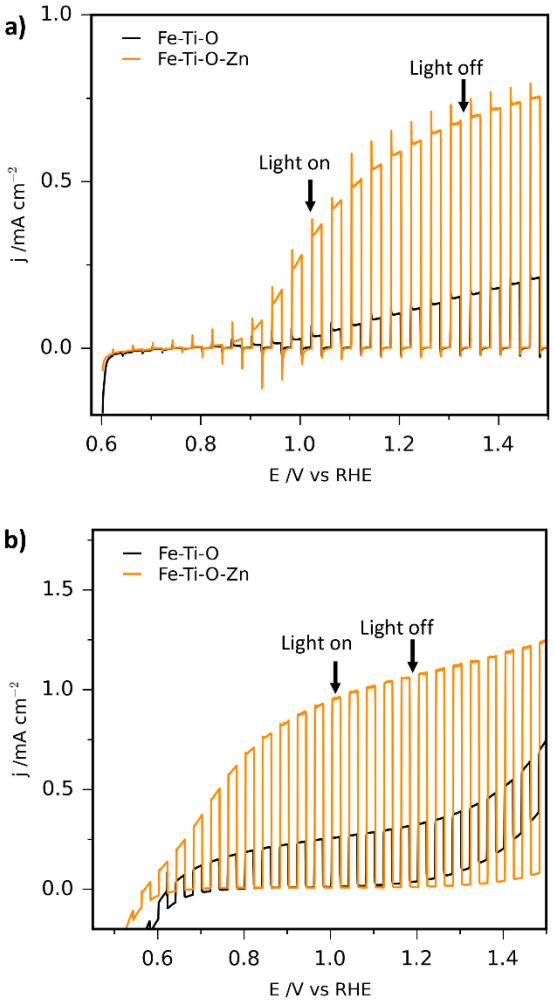

Figure 6. *j-V* curves of Fe-Ti-O-Zn and Fe-Ti-O, in (a) 1 mol L^{-1} NaOH (pH=13.6) and (b) 1 mol L^{-1} NaOH + 10 % (v/v) H_2O_2 (pH=11.9). All measurements were performed under chopped simulated sunlight (AM 1.5, 1 sun) and back-side illumination.

higher photocurrent performances have only been reported in systems that required the fabrication of more complex heterostructures such as the incorporation of metal oxides underlayers to prevent back electron injection from FTO to the electrolyte in porous electrodes combined with electrocatalysts on the surface for improved water oxidation kinetics. For example, H. Zhang *et al.* recently reported the highest performance to date, reaching photocurrent density values of 2.08 mA cm^{-2} at +1.23 V_{RHE} under simulated solar light.[55] The optimized system consisted of a Ga_2O_3 underlayer and $(Ni_2CoFe)OOH$ electrocatalyst on the surface. Previously, the same author also reported improved performance (0.93 mA cm^{-2}) on Fe_2TiO_5 systems that also required the use of a TiO_2 underlayer and the loading of a $FeNiO_x$ electrocatalyst.[56] Higher performances have also been achieved in systems where an ultrathin layer of Fe_2TiO_5 has been deposited on top of TiO_2 or Fe_2O_3 based photoanodes. However, in these systems Fe_2TiO_5 is not the major phase and hence they are not comparable.[16–18]

To further investigate the charge transport efficiencies, the PEC performances of the photoanodes were measured in the presence of H_2O_2 as a hole scavenger (Figure 6b). Under these conditions, photocurrent transients are not observed for all samples since most of the holes reaching the surface of the sample can be effectively transferred to the electrolyte to oxidize H_2O_2 due to its fast reaction kinetics. In the presence of H_2O_2, all photocurrent density values are higher confirming the scavenging effect of H_2O_2. Fe-Ti-O-Zn shows the highest photocurrent density value of 1.1 mA cm^{-2} at +1.23 V_{RHE}, which we attribute to the Zn doping of the Fe_2TiO_5 phase. The Fe-Ti-O sample achieves lower photocurrent density values of 0.3 mA cm^{-2} at +1.23 V_{RHE}. Charge injection efficiencies were calculated by the division of the photocurrent densities with and without H_2O_2 hole scavenger and the results are shown in Figure 7a.[25] Fe-Ti-O-Zn has the highest efficiency in the widest bias range, reaching a 60 % plateau beyond +1.35 V_{RHE}. A different trend is observed for Fe-Ti-O, in which the injection efficiency gradually increases as a function of applied bias without reaching a plateau. These two trends indicate that the applied potential is sufficient to suppress surface state recombination in the Fe-Ti-O-Zn sample, but not in the Fe-Ti-O, even at high applied bias.[57] At applied bias above 1.4 V_{RHE} charge injection efficiencies are higher in Fe-Ti-O than Fe-Ti-O-Zn, although the photocurrent performance (Figure 6a) is much lower at this potential. Since photocurrent performance depends on both charge injection and separation efficiencies, this trend suggests that charge separation efficiencies are higher for Fe-Ti-O-Zn at all the applied bias range studied (see below). Overall, the better injection efficiency values for Fe-Ti-O-Zn

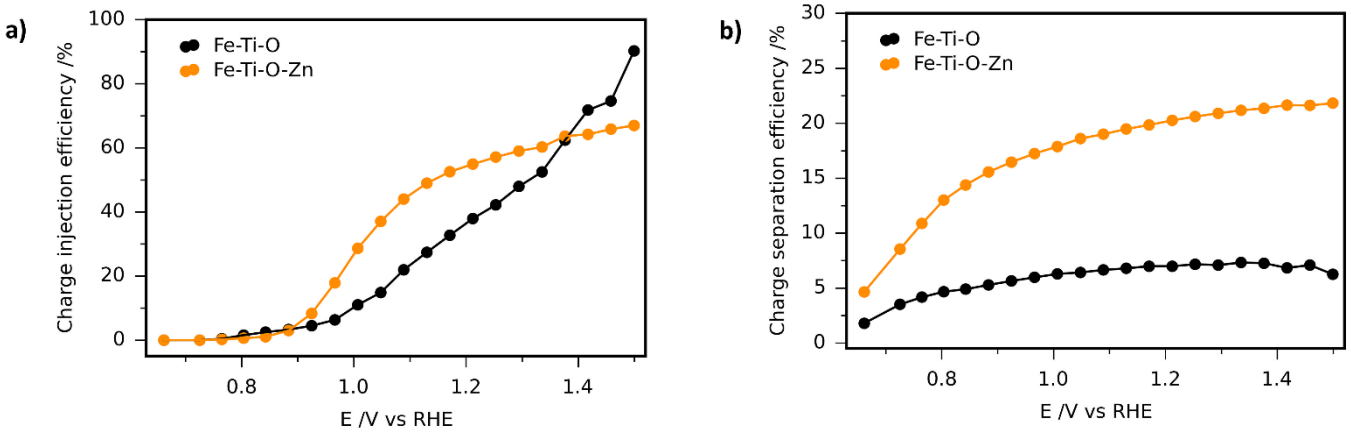

Figure 7. (a) Charge injection and (b) charge separation efficiencies of Fe-Ti-O-Zn and Fe-Ti-O.

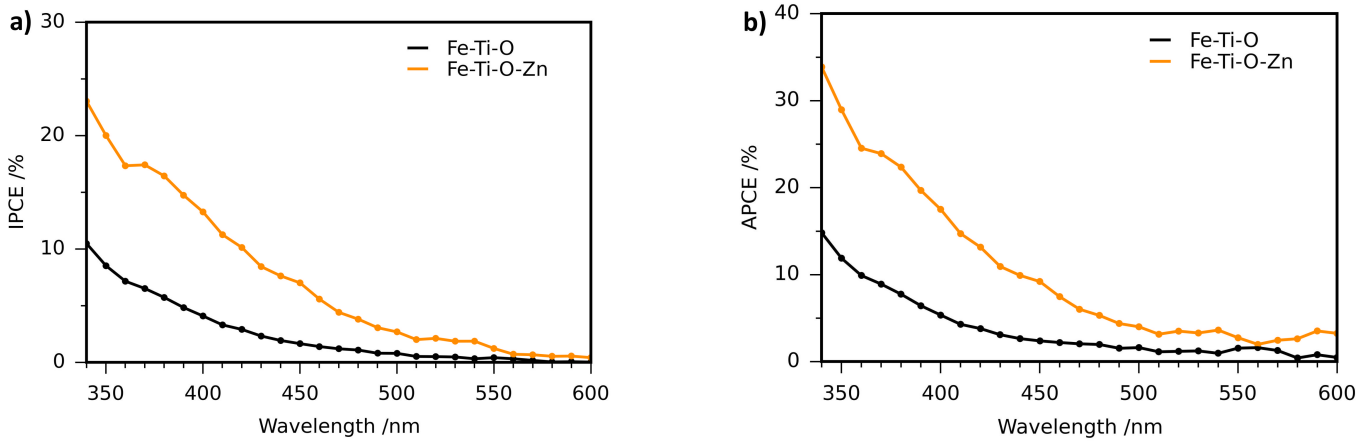

Figure 8. (a) IPCE and (b) APCE spectra of Fe-Ti-O and Fe-Ti-O-Zn. All measurements were performed in 1 mol L^{-1} NaOH (pH=13.6) and an applied potential of +1.23 V_{RHE}.

indicate either faster water oxidation kinetics or slower charge recombination at the surface of the photoanodes compared with Fe-Ti-O.[19,57,58]

The charge separation efficiency describes the ability of photogenerated holes to avoid bulk recombination and successfully reach the surface/electrolyte interface. The calculated values for the different photoanodes are shown in Figure 7b and the corresponding j_{abs} values are shown in Figure S9† and Table S2†. Fe-Ti-O-Zn achieves the highest separation efficiency values at all applied bias. The difference between Fe-Ti-O-Zn and Fe-Ti-O is remarkable, indicating that the incorporation of Zn^{2+} in the Fe_2TiO_5 lattice structure enhances bulk charge separation.

Photostability measurement at +1.23 V_{RHE} under simulated sunlight for Fe-Ti-O-Zn is shown in Figure S10†. Like in the *j-V* curves, an anodic transient appeared when the light was turned on and a cathodic transient when the light was turned off, indicating accumulation and dissipation of charges under these conditions.[59] Discarding the initial 200 s of stabilization, 80 % of the initial photocurrent was retained for 42 min. The photocurrent was recovered when the light was turned on and off. The observed decrease in photocurrent density over time in this alkaline electrolyte is most likely due to photocorrosion at the surface of the photoanode by accumulated holes.

IPCE values of Fe-Ti-O and Fe-Ti-O-Zn at +1.23 V_{RHE} are depicted in Figure 8a. Fe-Ti-O-Zn shows the highest IPCE performance, increasing gradually from 0.6 % at 590 nm to 23 % at 340 nm. Integration of the IPCE curves for Fe-Ti-O and Fe-Ti-O-Zn over the AM 1.5 solar spectrum results in a photocurrent density value of 0.19 and 0.62 mA cm^{-2}, respectively, being consistent with the measured photocurrent density values under simulated sunlight (see Figure 6a). As of PEC performances, this value is one of the highest IPCE values reported for Fe_2TiO_5 pseudobrookite based photoanodes (Table S1†). Calculated APCE values for Fe-Ti-O and Fe-Ti-O-Zn are shown in Figure 8b. Accordingly, the Fe-Ti-O-Zn sample shows the highest values that gradually increase from 4.0 % at 400 nm to 33.9 % at 340 nm. IPCE and APCE both confirm that Zn^{2+} incorporation in the Fe_2TiO_5 structure results in a superior utilization of the absorbed photons, in agreement with the improved charge separation efficiency.

ABPCE of photoanodes were also calculated and shown in Figure S11†. Fe-Ti-O-Zn exhibits the highest ABPCE efficiencies, reaching a maximum efficiency of 0.07 % at 1.04 V_{RHE} and outperforming by a factor of eight the highest Fe-Ti-O efficiency. This further confirms the positive impact that Zn incorporation on Fe-Ti-O has on improving PEC performances and photoconversion efficiencies.

EIS measurements under simulated solar light were performed to evaluate charge transfer process in the photoanodes. Figure 9a shows Nyquist plots of Fe-Ti-O and Fe-Ti-O-Zn samples along with the equivalent circuit used to fit the data. The circuit includes the pair R_1/CPE_1 that describes the semiconductor resistance and capacitance at the depletion layer, and the pair R_2/CPE_2 which describes the resistance and capacitance of the semiconductor at the Helmholtz layer of the photoanodes. R_s describes the series resistance of the cell.[55] The obtained fitted results indicate R_1 and R_2 values of 418.5 and 8,483 Ω for Fe-Ti-O, and 39.6 and 850.4 Ω for Fe-Ti-O-Zn, respectively . The smaller resistance values of Fe-Ti-O-Zn indicate a better separation efficiency and faster transfer rate for photogenerated charges at the electrode/electrolyte interface. This agrees well with the higher photocurrent performances and improved charge separation and injection efficiencies obtained for Fe-Ti-O-Zn photoanodes.

EIS measurements in the dark were carried out in the form of Mott-Schottky analysis to characterize the intrinsic properties of the photoanodes, such as the flat band potential (E_{FB}) and the carrier concentration (N_D). An ideal capacitive response, which is the pre-requisite for Mott-Schottky analysis, corresponding to a linear relation between log (Z'') *vs.* log (f) and log (Z') *vs.* log (f) with slopes of -1 and 0, respectively, was obtained at 100 Hz frequency (data not shown). Performing the Mott-Schottky analysis at this frequency allowed us to obtain accurate E_{FB} and N_D values. Mott-Schottky plots are shown in Figure 9d. Both plots indicate that all samples possess a positive slope, typical of n-type semiconductors.[60] The flat band potentials (E_{FB}) and electron carrier densities (N_D) for all samples are listed in Table 3. The incorporation of Zn^{2+} does not significantly modify the E_{FB} of Fe-Ti-O and Fe-Ti-O-Zn samples. However, Zn^{2+} doping remarkably increases the N_D values of Fe-Ti-O

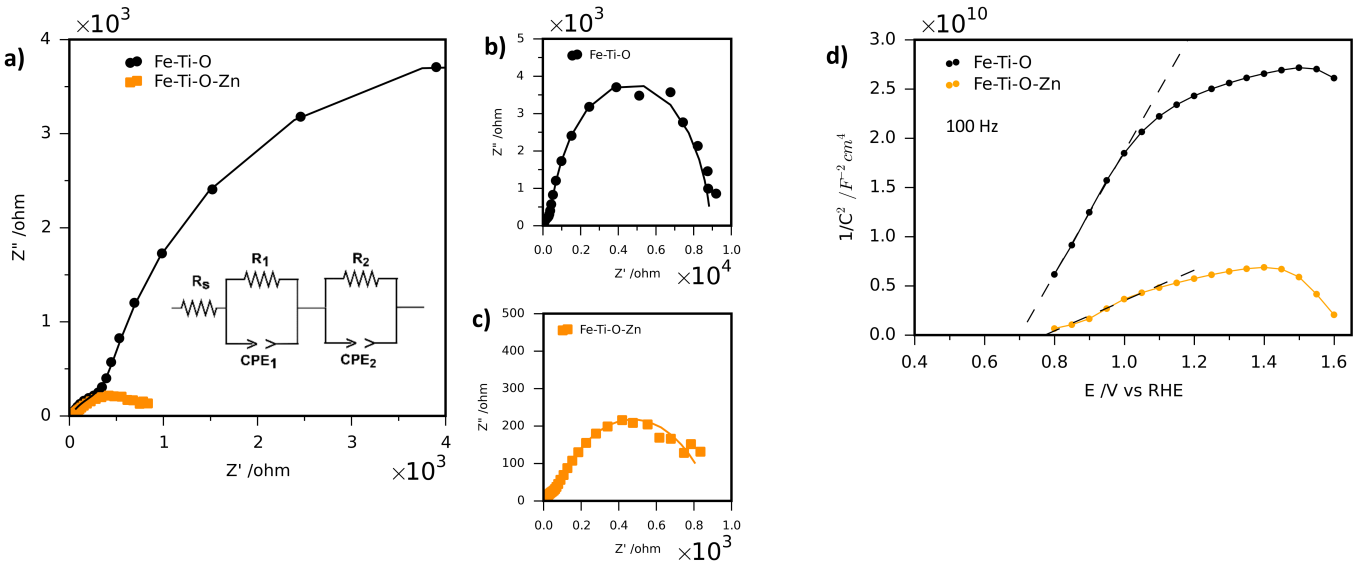

Figure 9. (a-c) Nyquist plots of Fe-Ti-O and Fe-Ti-O-Zn measured at +1.23 V_{RHE} under simulated solar light (AM 1.5G, 100 mW cm^{-2}). The equivalent circuit used to fit the data is shown in the inset of (a). (d) Mott-Schottky plots of Fe-Ti-O-Zn and Fe-Ti-O, measured at a fixed frequency of 100 Hz. All measurements were performed in 1 mol L^{-1} NaOH (pH=13.6).

from 2.1 x 10^{17} to 9.1 x 10^{17} cm^{-3}, evidencing improvement in charge transport and electrical conductivity.[60]

The enhancement in N_D values is initially a bit counter-intuitive since Zn^{2+} has lower valence than Ti^{4+} or Fe^{3+}, which is typically compensated by a reduction in the concentration of free electrons according to the following defect chemical equation (based on the Kröger-Vink notation):

$$Fe_2O_3 + ZnO + \frac{1}{2}O_2(g) + 2e' \xrightarrow{Fe_2TiO_5} 2Fe_{Fe}^{\times} + Zn_{Ti}'' + 5O_O^{\times} \quad (7)$$

Alternatively, the ionic compensation reaction may occur; in fact, this is far more likely to occur than the electronic compensation reaction, since the concentration of free electrons in the undoped films (2.1 x 10^{17} cm^{-3}) is about 3 orders of magnitude lower than the concentration of Zn dopant ions (few %). In the case of ionic compensation, Zn doping is charge-compensated by the formation of oxygen vacancies:

$$Fe_2O_3 + ZnO \xrightarrow{Fe_2TiO_5} 2Fe_{Fe}^{\times} + Zn_{Ti}'' + 4O_O^{\times} + V_O^{\cdot\cdot} \quad (8)$$

Note that while the presence of oxygen vacancies is normally associated with the presence of free electrons (which is indeed the case if an n-type oxide would be reduced in an oxygen-poor atmosphere), this is not the case here: for ZnO doping, the oxygen vacancies are compensated by the Zn acceptors, not by free electrons. This means that even though the presence of oxygen vacancies is suggested in our XPS analysis, this is not enough to explain the increase in N_D values for the Fe-Ti-O-Zn samples. The only way to explain an increase in the N_D values of Fe_2TiO_5 after Zn doping is to assume that the Zn ions occupy interstitial sites in the Fe_2TiO_5 lattice, as shown below:

$$Zn_{Zn}^{\times} + O_O^{\times} \xrightarrow{Fe_2TiO_5} Zn_i^{\cdot\cdot} + 2e' + \frac{1}{2}O_2(g) \quad (9)$$

We cannot *a priori* say which of the reactions (8) or (9) is more likely to occur. However, even if reaction (8) is energetically more favorable at low defect concentrations, this is likely to change as more and more charged defects ($V_O^{\cdot\cdot}$ and Zn_{Ti}'') are formed and the defects start to 'feel' each other. At some point, the compensation mechanism is likely to change to that of Eq. (9), which contains only one charged ionic point defect. From this point, one would indeed observe an increase in N_D values and electrical conductivity. The proposed switch in compensation mechanisms is consistent with the fact that we have ~10^{19} cm^{-3} (i.e., 0.11 at.%) of Zn in the film, yet the N_D is at least two orders of magnitude smaller. Furthermore, these observations are also in agreement with the observed cell lattice expansion after Zn^{2+} incorporation (Table 1), suggesting that interstitials (Eq. 9) are more dominant than oxygen vacancies (Eq. 8). Based on these considerations, we conclude that Zn^{2+} ions play a role in modifying the electrical conductivity of our Fe_2TiO_5 pseudobrookite-based films, contributing to an enhancement in the PEC performance.

Table 3. Charge carrier concentration and flat band potential obtained from Mott- Schottky analysis.

Sample	N_D (cm^{-3})	E_{FB} (RHE)
Fe-Ti-O	2.1 x 10^{17}	0.71
Fe-Ti-O-Zn	9.1 x 10^{17}	0.76

To further understand the effect of incorporating Zn^{2+} on the electronic properties of the material, UPS measurements were undertaken to calculate the position of the Fermi level (E_F) and valence band (VB). Figure S12a† and Figure S12b† show the UPS spectra with bias (U_{bias} = -2 V) and without bias for Fe-Ti-O and Fe-Ti-O-Zn. For comparison, UPS spectra of Fe-O (α-Fe_2O_3 films) and Fe-O-Zn (α-Fe_2O_3 films with Zn) are also shown. Figure S13† shows an expansion of the UPS spectra without applied bias (i.e., Figure S12b†) on a linear and logarithmic scale. It is clear that,

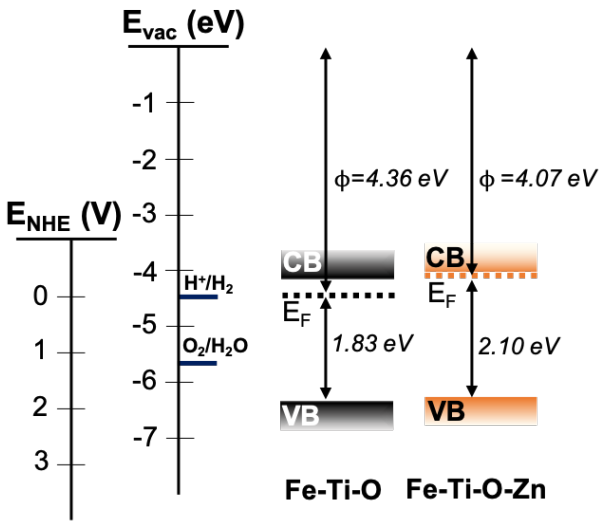

Figure 10. Schematic diagram of band level positions for Fe-Ti-O and Fe-Ti-O-Zn calculated from UPS measurements (Figure S12†) with respect to the vacuum level and the normal hydrogen electrode (NHE) potential.

especially from the logarithmic plot, Fe-Ti-O and Fe-Ti-O-Zn show a similar VB density-of-states pattern, and it is quite different from that of Fe-O and Fe-O-Zn. This indicates that the Fe-Ti-O films are clearly dominated by the Fe_2TiO_5 pseudobrookite phase, in spite of having some α-Fe_2O_3 present in the films as shown in XRD patterns (Figure 2a), allowing us to calculate the VBM by linear extrapolation for all samples.[61] The work function (ϕ) was calculated using the equation shown in the inset of Figure S12a†, and the results are tabulated in Table S3†.[62–64] The calculated values for all samples fall in the range of previously reported values.[10,65,66] From these values along with the UV-Vis absorptance spectra for the band-gap calculation (Figure 3 and Figure S14†), a schematic energy diagram was estimated and is represented in Figure 10 and Figure S15†. The CB and VB positions of both Fe-Ti-O and Fe-O systems agree with Fe_2TiO_5 and α-Fe_2O_3 values in literature.[10] This further confirms that Fe-Ti-O systems consist of a majority of Fe_2TiO_5 phase. Fe-Ti-O-Zn shows an upward shift of the E_F toward the CB in comparison with Fe-Ti-O agreeing with Mott-Schottky and N_D calculations, where higher N_D values are found for Fe-Ti-O-Zn. Higher carrier concentration (N_D) leads to an upward shift of the E_F and an increase in the electric field providing a higher density of electrons close to the CB, which can facilitate the charge separation at the semiconductor-electrolyte interface.[60,63,67] These differences in the E_F positions support that Zn^{2+} ions were efficiently incorporated into the crystal structure of Fe_2TiO_5, improving mainly its electrical conductivity.

CONCLUSIONS

In this work, we have demonstrated aerosol-assisted chemical vapor deposition of an Fe-Ti-O system and the impact of Zn^{2+} doping on its synthesis, crystallization and photoelectrochemical properties. We observed that Zn^{2+} doping boosts the formation of a Ti-rich Fe_2TiO_5 pseudobrookite phase over other secondary phases such as α-Fe_2O_3. Zn^{2+} incorporation preferentially occurs in the Fe_2TiO_5 phase over the α-Fe_2O_3 phase. It results in a 3-fold enhancement of the anodic photocurrent density values of prepared Fe_2TiO_5 pseudobrookite-based films, from *ca.* 0.2 to 0.6 mA cm^{-2} at+1.23 V_{RHE}. This is attributed to the better charge separation and injection efficiencies as observed in the resulting Zn-doped films. Mott-Schottky analysis reveals a significant increase in carrier concentration (N_D) upon Zn doping, which we attribute to Zn^{2+} ions occupying interstitial sites of the Fe_2TiO_5 pseudobrookite phase. Furthermore, ultraviolet photoelectron spectroscopy measurements show an upward shift of the Fermi level (E_F) after incorporation of Zn^{2+}, agreeing well with the observed higher N_D values. Overall, these results demonstrate a simple scalable chemical vapor methodology for the preparation of Zn-doped Fe_2TiO_5 pseudobrookite-based photoanodes with improved photoelectrochemical performance. These results prove the importance of doping ternary metal oxides, such as Fe_2TiO_5, for their selective formation and tailored electrical properties.

ASSOCIATED CONTENT

Supporting Information

The Supporting Information is available free of charge on the ACS Publications website.

Photograph of as-deposited films, XRD pattern, Raman spectra, SEM cross-sectional, survey XPS spectra, SEM-EDX spectrum, j-V curves, number of photons absorbed, photocurrent-time curve, UPS measurements, UV-Vis spectra and summary table with reported performances of Fe_2TiO_5 based photoanodes (PDF).

AUTHOR INFORMATION

Corresponding Author

* E-mail: prince.bassi@helmholtz-berlin.de
* E-mail: s.eslava@imperial.ac.uk

Author Contributions

The manuscript was written through contributions of all authors. All authors have given approval to the final version of the manuscript.

Notes

The authors declare no competing financial interest.

ACKNOWLEDGMENT

The authors would like to acknowledge both EPSRC for funding the Centre for Doctoral Training in Sustainable Chemical Technologies at the University of Bath (EP/L016354/1) and the Material and Chemical Characterisation facility (MC2) at the University of Bath. SE would like to acknowledge the financial support from an EPSRC Fellowship (EP/S030727/1). All data created during this research are openly available from the University of Bath data archive at https://doi.org/10.15125/BATH-00704.

REFERENCES

(1) Intergovernmental panel on climate change. *Summary for Policymakers of IPCC Special Report on Global Warming of 1.5 °C Approved by Governments*; 2018.

(2) World Energy Council. *Solar*; 2013.

(3) Fujishima, A.; Honda, K. TiO2 Photoelectrochemistry and Photocatalysis. *Nature* **1972**, *238*, 37–38.

(4) Gan, J.; Lu, X.; Tong, Y. Towards Highly Efficient Photoanodes: Boosting Sunlight-Driven Semiconductor Nanomaterials for Water Oxidation. *Nanoscale* **2014**, *6*, 7142–7164. https://doi.org/10.1039/c4nr01181c.

(5) Lianos, P. Review of Recent Trends in Photoelectrocatalytic Conversion of Solar Energy to Electricity and Hydrogen. *Appl. Catal. B Environ.* **2017**, *210*, 235–254. https://doi.org/10.1016/j.apcatb.2017.03.067.

(6) Li, J.; Wu, N. Semiconductor-Based Photocatalysts and Photoelectrochemical Cells for Solar Fuel Generation: A Review. *Catal. Sci. Technol.* **2015**, *5* (3), 1360–1384. https://doi.org/10.1039/C4CY00974F.

(7) Thalluri, S. M.; Bai, L.; Lv, C.; Huang, Z.; Hu, X.; Liu, L. Strategies for Semiconductor/Electrocatalyst Coupling toward Solar-Driven Water Splitting. *Adv. Sci.* **2020**, *7* (6), 1902102. https://doi.org/10.1002/advs.201902102.

(8) Niu, F.; Wang, D.; Li, F.; Liu, Y.; Shen, S.; Meyer, T. J. Hybrid Photoelectrochemical Water Splitting Systems: From Interface Design to System Assembly. *Adv. Energy Mater.* **2020**, *10* (11), 1900399. https://doi.org/10.1002/aenm.201900399.

(9) Gurudayal; Bassi, P. S.; Sritharan, T.; Wong, L. H. Recent Progress in Iron Oxide Based Photoanodes for Solar Water Splitting. *J. Phys. D. Appl. Phys.* **2018**, *51* (47), 473002. https://doi.org/10.1088/1361-6463/aae138.

(10) Bassi, P. S.; Chiam, S. Y.; Barber, J.; Wong, L. H. Hydrothermal Grown Nanoporous Iron Based Titanate, Fe 2 TiO 5 for Light Driven Water Splitting. *ACS Appl. Mater. Interfaces* **2014**, *24*, 2249–22495. https://doi.org/dx.doi.org/10.1021/am5065574.

(11) Courtin, E.; Baldinozzi, G.; Sougrati, M. T.; Stievano, L.; Sanchez, C.; Laberty-Robert, C. New Fe2TiO5-Based Nanoheterostructured Mesoporous Photoanodes with Improved Visible Light Photoresponses. *J. Mater. Chem. A* **2014**, *2* (18), 6567–6577. https://doi.org/10.1039/c4ta00102h.

(12) Bassi, P. S.; Xi, F.; Kölbach, M.; Gunder, R.; Ahmet, I. Y.; Krol, R. Van De; Fiechter, S. Pulsed Laser Deposited FeTiO Photoanodes for Photoelectrochemical Water Oxidation. *J. Phys. Chem. C* **2020**, *Just accep*. https://doi.org/10.1021/acs.jpcc.0c04396.

(13) Lee, D.; Baltazar, V. U.; Smart, T. J.; Ping, Y.; Choi, K. S. Electrochemical Oxidation of Metal-Catechol Complexes as a New Synthesis Route to the High-Quality Ternary Photoelectrodes: A Case Study of Fe2TiO5 Photoanodes. *ACS Appl. Mater. Interfaces* **2020**, *12*, 29275–29284. https://doi.org/10.1021/acsami.0c05359.

(14) Kuang, S.; Wang, M.; Geng, Z.; Wu, X.; Sun, Y.; Ma, W.; Chen, D.; Liu, J.; Feng, S.; Huang, K. Enhancement of Fe 2 TiO 5 Photoanode through Surface Al 3+ Treatment and FeOOH Modification . *ACS Sustain. Chem. Eng.* **2019**, *7* (17), 14347–14352. https://doi.org/10.1021/acssuschemeng.9b03425.

(15) Wang, M.; Wu, X.; Huang, K.; Sun, Y.; Zhang, Y.; Zhang, H.; He, J.; Chen, H.; Ding, J.; Feng, S. Enhanced Solar Water-Splitting Activity of Novel Nanostructured Fe2TiO5 Photoanode by Electro- Spray and Surface F-Modificatio. *Nanoscale* **2018**, *10*, 6678–6683. https://doi.org/10.1039/C8NR01331D.

(16) Liu, Q.; He, J.; Yao, T.; Sun, Z.; Cheng, W.; He, S.; Xie, Y.; Peng, Y.; Cheng, H.; Sun, Y.; Jiang, Y.; Hu, F.; Xie, Z.; Yan, W.; Pan, Z.; Wu, Z.; Wei, S. Aligned Fe 2 TiO 5 -Containing Nanotube Arrays with Low Onset Potential for Visible-Light Water Oxidation. *Nat. Commun.* **2014**, *5*, 5122. https://doi.org/10.1038/ncomms6122.

(17) Deng, J.; Lv, X.; Liu, J.; Zhang, H.; Nie, K.; Hong, C.; Wang, J.; Sun, X.; Zhong, J.; Lee, S.-T. Thin-Layer Fe 2 TiO 5 on Hematite for Efficient Solar Water Oxidation. *ACS Nano* **2015**, *9* (5), 5348–5356. https://doi.org/10.1021/acsnano.5b01028.

(18) Li, C.; Wang, T.; Luo, Z.; Liu, S.; Gong, J. Enhanced Charge Separation through ALD-Modified Fe 2 O 3 /Fe 2 TiO 5 Nanorod Heterojunction for Photoelectrochemical Water Oxidation. *Small* **2016**, *12* (25), 3415–3422. https://doi.org/10.1002/smll.201600940.

(19) Bassi, P. S.; Antony, R. P.; Boix, P. P.; Fang, Y.; Barber, J.; Wong, L. H. Crystalline Fe2O3/Fe2TiO5heterojunction Nanorods with Efficient Charge Separation and Hole Injection as Photoanode for Solar Water Oxidation. *Nano Energy* **2016**, *22*, 310–318. https://doi.org/10.1016/j.nanoen.2016.02.013.

(20) Hou, X.; Choy, K.-L. Processing and Applications of Aerosol-Assisted Chemical Vapor Deposition. *Chem. Vap. Depos.* **2006**, *12* (10), 583–596. https://doi.org/10.1002/cvde.200600033.

(21) Marchand, P.; Hassan, I. A.; Parkin, I. P.; Carmalt, C. J. Aerosol-Assisted Delivery of Precursors for Chemical Vapour Deposition: Expanding the Scope of CVD for Materials Fabrication. *Dalt. Trans.* **2013**, *42* (26), 9406–9422. https://doi.org/10.1039/c3dt50607j.

(22) Filho, P. I. O.; Carmalt, C. J.; Angeli, P.; Fraga, E. S. Mathematical Modeling for the Design and Scale-Up of a Large Industrial Aerosol-Assisted Chemical Vapor Deposition Process under Uncertainty. *Ind. Eng. Chem. Res.* **2020**, *59*, 1249–1260. https://doi.org/10.1021/acs.iecr.9b05869.

(23) Ahmet, I. Y.; Hill, M. S.; Johnson, A. L.; Peter, L. M. Polymorph-Selective Deposition of High Purity SnS Thin Films from a Single Source Precursor. *Chem. Mater.* **2015**, *27* (22), 7680–7688. https://doi.org/10.1021/acs.chemmater.5b03220.

(24) Regue, M.; Sibby, S.; Ahmet, I. Y.; Friedrich, D.; Abdi, F. F.; Johnson, A. L.; Eslava, S. TiO 2 Photoanodes with Exposed {0 1 0} Facets Grown by Aerosol-Assisted Chemical Vapor Deposition of a Titanium Oxo/Alkoxy Cluster. *J. Mater. Chem. A* **2019**, *7* (32), 19161–19172. https://doi.org/10.1039/C9TA04482E.

(25) Dotan, H.; Sivula, K.; Grätzel, M.; Rothschild, A.; Warren, S. C. Probing the Photoelectrochemical Properties of Hematite (α-Fe 2O3) Electrodes Using Hydrogen Peroxide as a Hole Scavenger. *Energy Environ. Sci.* **2011**, *4* (3), 958–964. https://doi.org/10.1039/c0ee00570c.

(26) Sivula, K.; Van De Krol, R. Semiconducting Materials for Photoelectrochemical Energy Conversion. *Nat. Rev. Mater.* **2016**, *1*, 15010. https://doi.org/10.1038/natrevmats.2015.10.

(27) Berry, F. J.; Greaves, C.; Helgason, Ö.; McManus, J.; Palmer, H. M.; Williams, R. T. Structural and Magnetic Properties of Sn-, Ti-, and Mg-Substituted α-Fe2o3: A Study by Neutron Diffraction and Mossbauer Spectroscopy. *J. Solid State Chem.* **2000**, *151* (2), 157–162. https://doi.org/10.1006/jssc.1999.8605.

(28) Yang, H.; Hazen, R. M. Crystal Chemistry of Cation Order–Disorder in Pseudobrookite-Type MgTi2 O5. *J. Solid State Chem.* **1998**, *138*, 238–244.

(29) Liermann, H. P.; Downs, R. T.; Yang, H. Site Disorder Revealed through Raman Spectra from Oriented Single Crystals: A Case Study on Karooite (MgTi2O5). *Am. Mineral.* **2006**, *91* (5–6), 790–793. https://doi.org/10.2138/am.2006.2027.

(30) He, M.; Winkler, B.; Bauer, J. D.; Bayarjargal, L.; Ruiz-Fuertes, J.; Alencar, I.; Morgenroth, W.; Refson, K.; Milman, V. Lattice Dynamics and Mg/Ti Order in Orthorhombic Pseudobrookite-Type MgTi2O5. *J. Alloys Compd.* **2017**, *699*, 16–24. https://doi.org/10.1016/j.jallcom.2016.12.217.

(31) Shannon, R. D. Revised Effective Ionic Radii and Systematic Studies of Interatomie Distances in Halides and Chaleogenides. *Acta Cryst.* **1976**, *A 32*, 751–767.

(32) Loan, T. T.; Huong, V. H.; Tham, V. T.; Long, N. N. Effect of Zinc Doping on the Bandgap and Photoluminescence of Zn2+-Doped TiO2 Nanowires. *Phys. B Condens. Matter* **2018**, *532* (December 2016), 210–215. https://doi.org/10.1016/j.physb.2017.05.027.

(33) Müller-Buschbaum, H.; Waburg, M. Pseudobrookite Mit Weitgehend Geordneter Metallverteilung : Ergebnisse. *Monatshefte für Chemie* **1983**, *114*, 21–25.

(34) Tiedemann, P.; Müller-Buschbaum, H. Zum Problem Der Metallverteilung in Pseudobrookiten: FeAlTiO5 Und Fe2TiO5. *Zeitschrift für Anorg. und Allg. Chemie* **1982**, *494*, 98–102. https://doi.org/10.1002/zaac.19824940112.

(35) Khatun, N.; Tiwari, S.; Vinod, C. P.; Tseng, C. M.; Wei Liu, S.; Biring, S.; Sen, S. Role of Oxygen Vacancies and Interstitials on Structural Phase Transition, Grain Growth, and Optical Properties of Ga Doped TiO2. *J. Appl. Phys.* **2018**, *123*, 245702. https://doi.org/10.1063/1.5027672.

(36) Yang, Y.; Yu, Y.; Wang, J.; Zheng, W.; Cao, Y. Doping and Transformation Mechanisms of Fe3+ Ions in Fe-Doped TiO2. *CrystEngComm* **2017**, *19* (7), 1100–1105. https://doi.org/10.1039/c6ce02523d.

(37) Bersani, D.; Lottici, P. P.; Montenero, A. Micro-Raman Study of Iron-Titanium Oxides Obtained by Sol-Gel Synthesis. *J. Mater. Sci.* **2000**, *35* (17), 4301–4305. https://doi.org/10.1023/A:1004884302755.

(38) Wang, L.; Nguyen, N. T.; Schmuki, P. A Facile Surface Passivation of Hematite Photoanodes with Iron Titanate Cocatalyst for Enhanced Water Splitting. *ChemSusChem* **2016**, *9* (16), 2048–2053. https://doi.org/10.1002/cssc.201600462.

(39) Wang, L.; Nguyen, N. T.; Huang, X.; Schmuki, P.; Bi, Y. Hematite Photoanodes: Synergetic Enhancement of Light Harvesting and Charge Management by Sandwiched with Fe2TiO5/Fe2O3/Pt Structures. *Adv. Funct. Mater.* **2017**, *27* (46), 1703527. https://doi.org/10.1002/adfm.201703527.

(40) Ahmmad, B.; Leonard, K.; Shariful Islam, M.; Kurawaki, J.; Muruganandham, M.; Ohkubo, T.; Kuroda, Y. Green Synthesis of Mesoporous Hematite (α-Fe2O 3) Nanoparticles and Their Photocatalytic Activity. *Adv. Powder Technol.* **2013**, *24* (1), 160–167. https://doi.org/10.1016/j.apt.2012.04.005.

(41) Lassoued, A.; Dkhil, B.; Gadri, A.; Ammar, S. Control of the Shape and Size of Iron Oxide (α-Fe2O3) Nanoparticles Synthesized through the Chemical Precipitation Method. *Results Phys.* **2017**, *7*, 3007–3015. https://doi.org/10.1016/j.rinp.2017.07.066.

(42) Wang, M.; Jiang, L.; Kim, E. J.; Hahn, S. H. Electronic Structure and Optical Properties of Zn(OH)2: LDA+U Calculations and Intense Yellow Luminescence. *RSC Adv.* **2015**, *5* (106), 87496–87503. https://doi.org/10.1039/c5ra17024a.

(43) Xiong, K.; Wang, K.; Chen, L.; Wang, X.; Fan, Q.; Courtois, J.; Liu, Y.; Tuo, X.; Yan, M. Heterostructured ZnFe2O4/Fe2TiO5/TiO2 Composite Nanotube Arrays with an Improved Photocatalysis Degradation Efficiency Under Simulated Sunlight Irradiation. *Nano-Micro Lett.* **2018**, *10:17*. https://doi.org/10.1007/s40820-017-0169-x.

(44) Biesinger, M. C.; Lau, L. W. M.; Gerson, A. R.; Smart, R. S. C. Resolving Surface Chemical States in XPS Analysis of First Row Transition Metals, Oxides and Hydroxides: Sc, Ti, V, Cu and Zn. *Appl. Surf. Sci.* **2010**, *257* (3), 887–898. https://doi.org/10.1016/j.apsusc.2010.07.086.

(45) Zhao, Y.; Li, C.; Liu, X.; Gu, F.; Du, H. L.; Shi, L. Zn-Doped TiO2 Nanoparticles with High Photocatalytic Activity Synthesized by Hydrogen-Oxygen Diffusion Flame. *Appl. Catal. B Environ.* **2008**, *79* (3), 208–215. https://doi.org/10.1016/j.apcatb.2007.09.044.

(46) Bharti, B.; Kumar, S.; Lee, H.-N.; Kumar, R. Formation of Oxygen Vacancies and Ti3+ State in TiO2 Thin Film and Enhanced Optical Properties by Air Plasma Treatment. *Sci. Rep.* **2016**, *6* (1), 32355. https://doi.org/10.1038/srep32355.

(47) McIntyre, N. S.; Zetaruk, D. G. X-Ray Photoelectron Spectroscopic Studies of Iron Oxides. *Anal. Chem.* **1977**, *49* (11), 1521–1529. https://doi.org/10.1021/ac50019a016.

(48) Mirbagheri, N.; Wang, D.; Peng, C.; Wang, J.; Huang, Q.; Fan, C.; Ferapontova, E. E. Visible Light Driven Photoelectrochemical Water Oxidation by Zn- and Ti-Doped Hematite Nanostructures. *ACS Catal.* **2014**, *4* (6), 2006–2015. https://doi.org/10.1021/cs500372v.

(49) Molina-Mendoza, A. J.; Giovanelli, E.; Paz, W. S.; Ninõ, M. A.; Island, J. O.; Evangeli, C.; Aballe, L.; Foerster, M.; Van Der Zant, H. S. J.; Rubio-Bollinger, G.; Agraït, N.; Palacios, J. J.; Pérez, E. M.; Castellanos-Gomez, A. Franckeite as a Naturally Occurring van Der Waals Heterostructure. *Nat. Commun.* **2017**, *8*, 14409. https://doi.org/10.1038/ncomms14409.

(50) Srivastava, M.; Alla, S. K.; Meena, S. S.; Gupta, N.; Mandal, R. K.; Prasad, N. K. ZnXFe3-XO4 (0.01 ≤ x ≤ 0.8) Nanoparticles for Controlled Magnetic Hyperthermia Application. *New J. Chem.* **2018**, *42* (9), 7144–7153. https://doi.org/10.1039/c8nj00547h.

(51) Farsinezhad, S.; Sharma, H.; Shankar, K. Interfacial Band Alignment for Photocatalytic Charge Separation in TiO2 Nanotube Arrays Coated with CuPt Nanoparticles. *Phys. Chem. Chem. Phys.* **2015**, *17* (44), 29723–29733. https://doi.org/10.1039/c5cp05679a.

(52) Gupta, R.; Sen, S.; Phase, D. M.; Avasthi, D. K.; Gupta, A. Tailoring Optical Properties of TiO 2 -Cr Co-Sputtered Films Using Swift Heavy Ions. *Appl. Surf. Sci.* **2018**, *440*, 403–408. https://doi.org/10.1016/j.apsusc.2018.01.003.

(53) Gleason-Rohrer, D. C.; Brunschwig, B. S.; Lewis, N. S. Measurement of the Band Bending and Surface Dipole at Chemically Functionalized Si(111)/Vacuum Interfaces. *J. Phys. Chem. C* **2013**, *117* (35), 18031–18042. https://doi.org/10.1021/jp401585s.

(54) Krol, R. Van De; Grätzel, M. *Photoelectrochemical Hydrogen Production*; Springer US, 2012. https://doi.org/10.1007/978-1-4614-1380-6.

(55) Zhang, H.; Park, S. O.; Joo, S. H.; Kim, J. H.; Kwak, S. K.; Lee, J. S. Precisely-Controlled, a Few Layers of Iron Titanate Inverse Opal Structure for Enhanced Photoelectrochemical Water Splitting. *Nano Energy* **2019**, *62*, 20–29. https://doi.org/10.1016/j.nanoen.2019.05.025.

(56) Zhang, H.; Kim, J. H.; Kim, J. H.; Lee, J. S. Engineering Highly Ordered Iron Titanate Nanotube Array Photoanodes for Enhanced Solar Water Splitting Activity. *Adv. Funct. Mater.* **2017**, *27* (35), 1–9. https://doi.org/10.1002/adfm.201702428.

(57) Liardet, L.; Katz, J. E.; Luo, J.; Grätzel, M.; Hu, X. An Ultrathin Cobalt–Iron Oxide Catalyst for Water Oxidation on Nanostructured Hematite Photoanodes. *J. Mater. Chem. A*

2019, 6012–6020. https://doi.org/10.1039/C8TA12295D.

(58) Luo, Z.; Li, C.; Liu, S.; Wang, T.; Gong, J. Gradient Doping of Phosphorus in Fe2O3 Nanoarray Photoanodes for Enhanced Charge Separation. *Chem. Sci.* **2017**, *8* (1), 91–100. https://doi.org/10.1039/c6sc03707k.

(59) Le Formal, F.; Sivula, K.; Grätzel, M. The Transient Photocurrent and Photovoltage Behavior of a Hematite Photoanode under Working Conditions and the Influence of Surface Treatments. *J. Phys. Chem. C* **2012**, *116* (51), 26707–26720. https://doi.org/10.1021/jp308591k.

(60) Zhang, Z.; Wang, P. Optimization of Photoelectrochemical Water Splitting Performance on Hierarchical TiO2 Nanotube Arrays. *Energy Environ. Sci.* **2012**, *5* (4), 6506–6512. https://doi.org/10.1039/c2ee03461a.

(61) Zhang, Y.; Lin, N.; Li, Y.; Wang, X.; Wang, H.; Kang, J.; Wilks, R.; Bär, M.; Mu, R. The Isotype ZnO/SiC Heterojunction Prepared by Molecular Beam Epitaxy - A Chemical Inert Interface with Significant Band Discontinuities. *Sci. Rep.* **2016**, *6*, 23106. https://doi.org/10.1038/srep23106.

(62) Gao, J.; Perkins, C. L.; Luther, J. M.; Hanna, M. C.; Chen, H. Y.; Semonin, O. E.; Nozik, A. J.; Ellingson, R. J.; Beard, M. C. N-Type Transition Metal Oxide as a Hole Extraction Layer in PbS Quantum Dot Solar Cells. *Nano Lett.* **2011**, *11* (8), 3263–3266. https://doi.org/10.1021/nl2015729.

(63) Su, C. Y.; Wang, L. C.; Liu, W. S.; Wang, C. C.; Perng, T. P. Photocatalysis and Hydrogen Evolution of Al- and Zn-Doped TiO2 Nanotubes Fabricated by Atomic Layer Deposition. *ACS Appl. Mater. Interfaces* **2018**, *10* (39), 33287–33295. https://doi.org/10.1021/acsami.8b12299.

(64) Kölbach, M.; Pereira, I. J.; Harbauer, K.; Plate, P.; Höflich, K.; Berglund, S. P.; Friedrich, D.; Van De Krol, R.; Abdi, F. F. Revealing the Performance-Limiting Factors in α-SnWO4 Photoanodes for Solar Water Splitting. *Chem. Mater.* **2018**, *30* (22), 8322–8331. https://doi.org/10.1021/acs.chemmater.8b03883.

(65) Kraushofer, F.; Jakub, Z.; Bichler, M.; Hulva, J.; Drmota, P.; Weinold, M.; Schmid, M.; Setvin, M.; Diebold, U.; Blaha, P.; Parkinson, G. S. Atomic-Scale Structure of the Hematite α-Fe2O3(11-02) 'r-Cut' Surface. *J. Phys. Chem. C* **2018**, *122* (3), 1657–1669. https://doi.org/10.1021/acs.jpcc.7b10515.

(66) Kment, S.; Riboni, F.; Pausova, S.; Wang, L.; Wang, L.; Han, H.; Hubicka, Z.; Krysa, J.; Schmuki, P.; Zboril, R. Photoanodes Based on TiO2 and α-Fe2O3 for Solar Water Splitting-Superior Role of 1D Nanoarchitectures and of Combined Heterostructures. *Chem. Soc. Rev.* **2017**, *46* (12), 3716–3769. https://doi.org/10.1039/c6cs00015k.

(67) Zhu, F.; Zhang, P.; Wu, X.; Fu, L.; Zhang, J.; Xu, D. The Origin of Higher Open-Circuit Voltage in Zn-Doped TiO 2 Nanoparticle-Based Dye-Sensitized Solar Cells. *ChemPhysChem* **2012**, *13* (16), 3731–3737. https://doi.org/10.1002/cphc.201200362.

Authors are required to submit a graphic entry for the Table of Contents (TOC) that, in conjunction with the manuscript title, should give the reader a representative idea of one of the following: A key structure, reaction, equation, concept, or theorem, etc., that is discussed in the manuscript. Consult the journal's Instructions for Authors for TOC graphic specifications.